

Geophysical Research Letters



RESEARCH LETTER

10.1029/2023GL107392

Key Points:

- Two Interplanetary shock events in the lunar environment are analyzed to unveil whistler wave generation around shock region
- Linear wave growth calculations show that whistler-mode waves are generated locally due to enhanced electron anisotropy and flux
- Magnetic field line connection to lunar surface is found to be important for enhancing whistler wave intensity

Supporting Information:

Supporting Information may be found in the online version of this article.

Correspondence to:

A. Prasad and W. Li, abhi99@bu.edu; wenli77@bu.edu

Citation:

Prasad, A., Li, W., Ma, Q., & Shen, X.-C. (2024). Whistler-mode wave generation during interplanetary shock events in the Earth's lunar plasma environment. *Geophysical Research Letters*, 51, e2023GL107392. https://doi.org/10.1029/2023GL107392

Received 20 NOV 2023 Accepted 8 APR 2024

© 2024. The Authors. This is an open access article under the terms of the Creative Commons Attribution License, which permits use, distribution and reproduction in any medium, provided the original work is properly cited.

Whistler-Mode Wave Generation During Interplanetary Shock Events in the Earth's Lunar Plasma Environment

Abhinav Prasad¹, Wen Li¹, Qianli Ma^{1,2}, and Xiao-Chen Shen¹

¹Astronomy Department, Center for Space Physics, Boston University, Boston, MA, USA, ²Department of Atmospheric and Oceanic Sciences, University of California, Los Angeles, CA, USA

Abstract Whistler-mode waves are commonly observed within the lunar environment, while their variations during Interplanetary (IP) shocks are not fully understood yet. In this paper, we analyze two IP shock events observed by Acceleration, Reconnection, Turbulence and Electrodynamics of the Moons Interaction with the Sun (ARTEMIS) satellites while the Moon was exposed to the solar wind. In the first event, ARTEMIS detected whistler-mode wave intensification, accompanied by sharply increased hot electron flux and anisotropy across the shock ramp. The potential reflection or backscattering of electrons by the lunar crustal magnetic field is found to be favorable for whistler-mode wave intensification. In the second event, a magnetic field line rotation around the shock region was observed and correlated with whistler-mode wave intensification. The wave growth rates calculated using linear theory agree well with the observed wave spectra. Our study highlights the significance of magnetic field variations and anisotropic hot electron distributions in generating whistler-mode waves in the lunar plasma environment following IP shock arrivals.

Plain Language Summary The surface of the Earth's Moon is frequently exposed to the incoming solar wind flow and IP shocks due to its lack of internal magnetic fields that can deflect the solar wind particles. Within the lunar environment, whistler-mode waves, characterized by electromagnetic fluctuations with frequencies below the electron gyrofrequency, are commonly present. Interplanetary shocks that are often associated with significant disturbances in electron flux and magnetic field can potentially lead to anisotropic distributions of electrons, which are known to provide free energy source for whistler-mode wave generation. To assess the whistler wave generation under shock conditions, we conduct an in-depth analysis of two IP shock events. These events provide clear evidence of shock-induced enhancements in electron pitch angle anisotropy and flux, as well as a potential rotation of magnetic field around the shock region, resulting in the intensification of whistler-mode waves downstream of the shock. We calculated a timeseries of linear wave growth rate for the entire duration of shock events, which remarkably accounted for the observed whistler-mode wave spectra both before and after the shock arrival. Our findings are important for understanding the associated physical process of whistler-mode wave generation in the lunar plasma environment during IP shock events.

1. Introduction

The Earth's Moon lacks an internal global magnetic field, leaving its surface exposed to the surrounding plasma conditions (Halekas et al., 2011). Throughout its orbit around the Earth, the Moon encounters a range of plasma conditions originating from the solar wind and the terrestrial magnetosphere, resulting in diverse moon-plasma interactions (Harada & Halekas, 2016; Nakagawa, 2016). The lunar surface also has a sparse distribution of crustal magnetic fields, which often serve as hotspots of intense plasma wave activity (Halekas, Brain, Mitchell, & Lin, 2006; Harada et al., 2014). One of the most ubiquitously observed waves in the lunar environment are whistler-mode waves, which are right-hand polarized electromagnetic fluctuations with frequencies below the electron gyrofrequency (f_{ce}) (Harada et al., 2015; Sawaguchi et al., 2022). Multiple plasma interactions contribute to whistler-mode wave generation in the lunar environment. On the dayside, the lunar surface is exposed to streaming solar wind ions and electrons, some of which are reflected or backscattered from the lunar surface, forming a loss cone structure and anisotropic electron pitch angle distribution, which could possibly generate whistler-mode waves (Halekas et al., 2012; Halekas, Brain, Mitchell, Lin, & Harrison, 2006; Harada et al., 2014; Nakagawa et al., 2011; Tsugawa et al., 2011). On the nightside, a lunar wake is formed that has a layered structure of electric potential which can reflect the electrons with low parallel velocities and cause magnetic drift, thus leading to an anisotropic electron pitch angle distribution favorable for whistler-mode wave generation (Fatemi et al., 2013; Halekas, 2005; Nakagawa & Iizima, 2005).

PRASAD ET AL.

The Acceleration, Reconnection, Turbulence and Electrodynamics of the Moons Interaction with the Sun (ARTEMIS) mission has been providing in-situ wave and particle measurements from the lunar environment for more than a decade (Angelopoulos, 2011), and has provided complete coverage in the lunar plasma environment within a distance of 11 lunar radii (R_L). Several observational and theoretical studies analyzed the ARTEMIS data to provide insights into the characteristics of whistler-mode waves in the lunar environment (Harada et al., 2014, 2015; Sawaguchi et al., 2021), Studies have also identified the key parameters affecting whistler-mode wave generation, such as the presence of lunar crustal magnetic field (Harada et al., 2014), connection of IP magnetic field to the lunar surface (Sawaguchi et al., 2022), electron temperature anisotropy (Tong, Vasko, Pulupa, et al., 2019), and solar wind speed (Tong, Vasko, Artemyev, et al., 2019).

Interplanetary shocks are known to often lead to a number of plasma perturbations (e.g., Kajdič et al., 2014). In particular, whistler-mode waves are frequently observed downstream of the shock ramp (Kajdič et al., 2012; Russell et al., 2009; Wilson et al., 2013). Davis et al. (2021) analyzed 11 IP shocks observed around lunar environment by ARTEMIS and evaluated the wave occurrence rates around the shock region. However, it remains unclear whether the plasma environment and electron distributions during IP shock events locally generate whistler-mode waves.

In this paper, we conduct an in-depth analysis of two IP shock events observed by the dual ARTEMIS probes to evaluate whistler-mode wave generation in the vicinity of the Moon. We further use linear theory to calculate the wave growth rates, and compare them with the observed whistler-mode wave spectra.

2. Observations of Interplanetary Shock Events

We examine IP shock events observed by the two ARTEMIS probes (Angelopoulos, 2011) in lunar environment. Hereafter the two ARTEMIS probes are referred to as P1 and P2. We use the particle measurements from the Electrostatic Analyzer (ESA) instrument. For the electromagnetic fields data, we use the measurements from the Fluxgate Magnetometer (FGM), Search Coil Magnetometer (SCM) and Electric Field Instrument (EFI) (Auster et al., 2008; Bonnell et al., 2008; Roux et al., 2008). In addition, we use the field and particle observations from the WIND spacecraft (Harten & Clark, 1995; Lepping et al., 1995; Lin et al., 2021) to obtain solar wind measurements near the Sun-Earth Lagrange-1 (L1) point.

Figure 1 shows the first IP shock event observed simultaneously by the two ARTEMIS probes on 15 March 2023. During this event, the Moon was in the solar wind and on the dawnside of Earth. The trajectories of both probes in selenographic solar ecliptic (SSE) coordinates are shown in Figure 1v during the event. In the SSE coordinates, the positive X axis points from the Moon toward the Sun, Z axis is along the northward normal of the Earth's ecliptic plane, and Y axis completes the orthogonal system. P2 was located relatively closer to the lunar surface (at roughly $0.5\,R_L$) compared to P1, which was located further away at a distance of $10\,R_L$. The relative closeness of P2 is also reflected by the fact that the background magnetic field is connected to the lunar surface (indicated by the bottom colorbar in Figure 1) with an orientation pointing toward the surface (also see Figure S1 in Supporting Information S1). The magnetic field connection to the lunar surface is inferred by assuming a straight magnetic field line geometry. The background magnetic field measured by P1 was completely disconnected throughout the entire duration of event. The IP shock arrival was recorded by both probes at around 04:32:00 UT, as indicated by the sharp gradients in the background magnetic field (Figures 1a and 1j), electron and ion number density (Figures 1b and 1k) and solar wind dynamic pressure (Figures 1c and 1l). The IP shock was also recorded by the WIND spacecraft prior to the ARTEMIS probes at around 04:02:00 UT, as indicated similarly by the sharp gradient in measured magnetic field (in geocentric solar ecliptic coordinates), solar wind density, and solar wind flow speed (Figures 1s-1u). Figures 1i and 1r show that downstream of the shock ramp, strong magnetic wave amplitudes were simultaneously recorded by both ARTEMIS probes. Using the SCM waveform data available from P2, we confirmed that the waves above 50 Hz measured downstream of the shock are whistler-mode waves (see Figure S2 in Supporting Information S1). Moreover, the angle between wave vector and background magnetic field (wave normal angle) for the whistler-mode waves was found to be close to 0°. Interestingly, during 04:19:00-04:41:00 UT, P2 recorded whistler-mode wave amplitudes downstream of the shock that were an order of magnitude higher compared to P1. This difference can be attributed to the fact that the magnetic field line was connected to the lunar surface for P2, thus increasing the likelihood of interactions between incoming shockdriven electrons and lunar crustal magnetic field sources, forming an anisotropic distribution favorable for whistler-mode wave generation (Gurnett & Bhattacharjee, 2017; Kennel, 1966). Both probes recorded a sharp

PRASAD ET AL. 2 of 9

19448007, 2024, 10, Downloaded from https://agupubs.onlinelibrary.wiley.com/doi/10.1029/2023G1.07392 by Boston University, Wiley Online Library on [31/05/2025]. See the Terms and Conditions (https://onlinelibrary.wiley.com/terms-and-

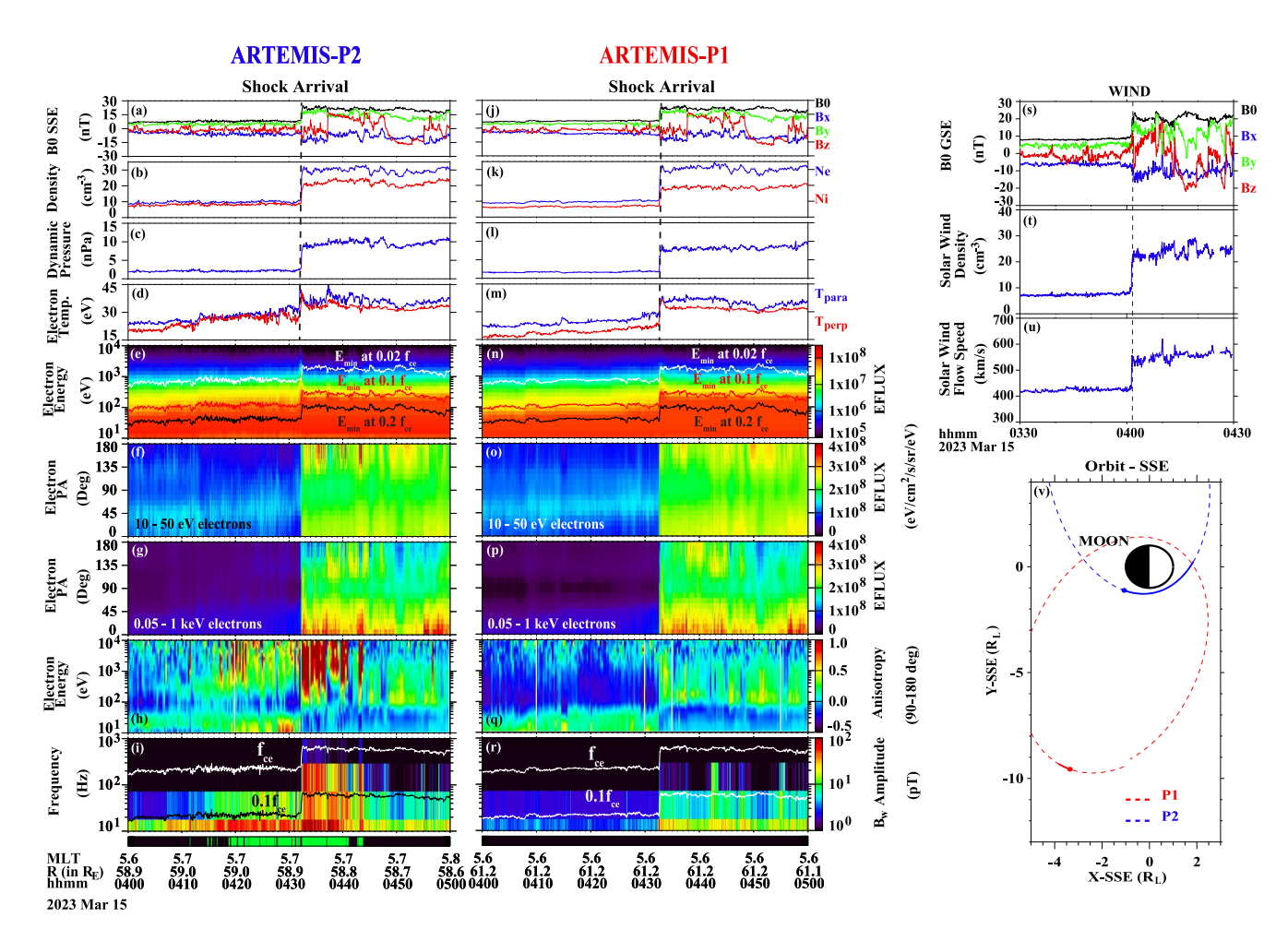


Figure 1. Summary plot of the Interplanetary shock event observed on 15 March 2023 (a), (j) Background magnetic field and its three components in the selenographic solar ecliptic (SSE) coordinates (b), (k) electron and ion number density (c, l) solar wind dynamic pressure (d, m) parallel and perpendicular electron temperature (e, n) energy spectrogram of electron energy flux (the white, red and black lines correspond to the minimum resonance energies for the given wave frequencies) (f, g, o, p) pitch angle spectrogram of electron energy flux for 10–50 eV and 0.05–1 keV electrons (h, q) energy spectrogram of electron anisotropy for 90°–180° pitch angle (i, r) frequency spectrogram of magnetic wave amplitude; colorbars at the bottom of figure are the indicator of background magnetic field connection to Moon (black: no connection; green: connection with field pointing toward the lunar surface; red: connection with field pointing away from the surface) (s, t, and u) WIND measurements of magnetic field and its three components in geocentric solar ecliptic coordinates, solar wind density and flow speed; and (v) trajectories of Acceleration, Reconnection, Turbulence and Electrodynamics of the Moons Interaction with the Sun probes in SSE coordinates.

increase in the electron energy flux across the shock ramp (Figures 1e and 1n). The electron pitch angle spectrogram of energy flux from both probes indicates that across the shock ramp, energy flux of 50 eV–1 keV electrons increases at all pitch angles for P1 and P2, but with a more significant increase near 0° pitch angle (Figures 1g and 1p). Moreover, the 50 eV–1 keV electron flux at pitch angles near 180° is smaller than that at other pitch angles, as observed by P2 during 04:20:00–04:40:00 UT (Figure 1g), when magnetically connected to the Moon. This is because the magnetic field lines measured by P2 were connected and pointing toward the lunar surface, thus the incoming electrons traveling along field lines were either absorbed by the lunar surface or reflected/backscattered from the lunar crustal sources. P2 also observed a higher flux of low energy (<50 eV) electrons near 180° pitch angle just after the shock arrival (04:32–04:36 UT), which could result from an upward accelerated electron beam due to reflection from the lunar surface (Figure 1f). A similar example of different pitch angle distributions for low and high energy electrons around the lunar surface was previously reported by Harada et al. (2014) in events not involving IP shocks.

Based on the electron pitch angle distribution measurements, we calculated the anisotropy at various energies (Figures 1h and 1q), using the equation below (Chen et al., 1999).

PRASAD ET AL. 3 of 9

19448007, 2024, 10, Downloaded from https://agupubs.onlinelibrary.wiley.com/doi/10.1029/2023GL107392 by Boston University, Wiley Online Library on [31/05/2025]. See the Terms and Conditions (https://onlineli

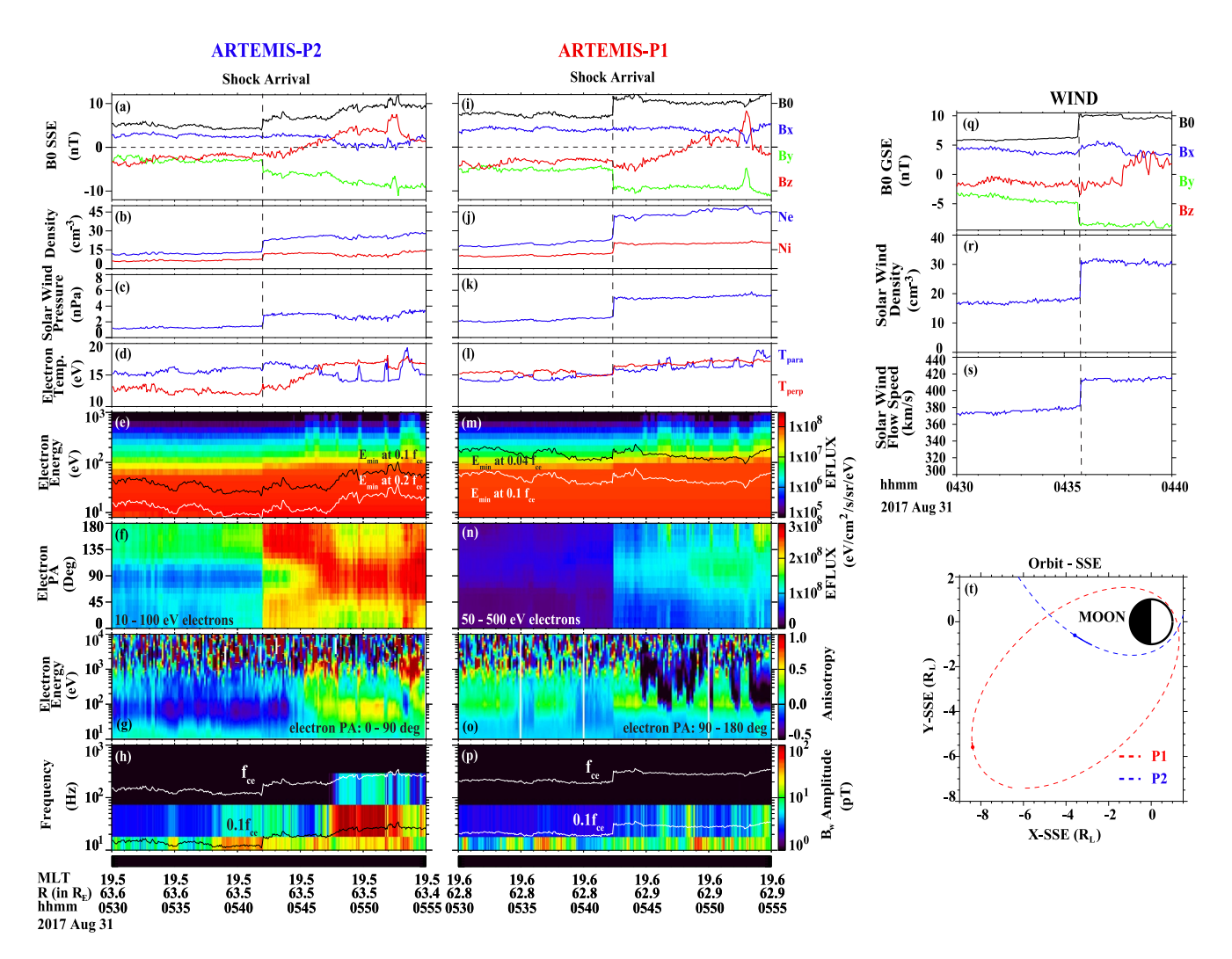


Figure 2. Summary plot of the Interplanetary shock event observed on 31 August 2017. The figure format is the same as Figure 1, except that the energy range is 10-100 eV in panel (f) and 50-500 eV in panel (n), and the pitch angle range used to calculate electron pitch angle anisotropy is $0^{\circ}-90^{\circ}$ in panel (g) and $90^{\circ}-180^{\circ}$ in panel (o).

$$A_{\alpha_1-\alpha_2} = \frac{\int_{\alpha_1}^{\alpha_2} f(E,\alpha) \sin^3 \alpha \, d\alpha}{2 \int_{\alpha_1}^{\alpha_2} f(E,\alpha) \cos^2 \alpha \sin \alpha \, d\alpha} - 1, \text{ for } \alpha_1 = 0^\circ \text{ and } \alpha_2 = 90^\circ, \text{ or } \alpha_1 = 90^\circ \text{ and } \alpha_2 = 180^\circ$$

Here $A_{\alpha_1-\alpha_2}$ is the anisotropy for electrons with energy (E) and pitch angles (α) between α_1 and α_2 , and f is the electron phase space density (PSD). The anisotropy is defined such that positive, 0, and negative values correspond to pancake, isotropic, and field-aligned pitch angle distributions at a given energy. In Figures 1h and 1q, we calculated the anisotropy for electrons with pitch angles over $90^{\circ}-180^{\circ}$, since these electrons can play a significant role in generating quasi-parallel whistler-mode waves (Gurnett & Bhattacharjee, 2017; Kennel, 1966). The electron anisotropy increased (decreased) across the shock ramp for both probes at energies above (below) $\sim 50 \text{ eV}$. Both P2 and P1 recorded a higher anisotropy at energies above 50 eV (Figures 1h and 1q) downstream of shock, which is highly correlated with the enhanced whistler-mode waves (Figures 1i and 1r). The lower-energy electrons exhibited a field-aligned distribution after the shock arrival, which is consistent with $T_{\text{para}} > T_{\text{perp}}$ shown in Figures 1d and 1m.

Figure 2 presents a summary plot during another IP shock event that occurred on 31 August 2017. The IP shock was recorded by both probes, when the Moon was in the solar wind on the Earth's duskside. The IP shock was recorded at around 05:42:00 UT, as shown by the sharp gradient in background magnetic field (Figures 2a and 2i),

PRASAD ET AL. 4 of 9

electron and ion number density (Figures 2b and 2j), and solar wind pressure (Figures 2c and 2k). The WIND spacecraft also recorded the IP shock at around 04:36:00 UT (Figure 2q-2s). The trajectories of ARTEMIS probes show that P2 was relatively closer to the lunar surface compared to P1 (Figure 2t). However, linear extrapolation of background magnetic field shows that neither of the probes were connected to the lunar surface (indicated by the bottom colored bars in Figure 2). P2 observed strong waves (Figure 2h) downstream of the shock during 05:46:30-05:53:00 UT, which is strongly correlated with a shift in the pitch angle distribution of 10-100 eV electrons toward 90° (Figure 2f). The sudden intensification of waves coincided with a change in the orientation of background magnetic field, as reflected by the Bz change from negative to positive values (Figure 2a). It is noteworthy that the magnetic field line rotation feature was also detected by WIND at ~04:38:00 UT (Figure 2q), suggesting the existence of a magnetic field line rotation around the shock region. However, the precise mechanism underlying the observed rotation of the magnetic field downstream of the shock ramp and the associated change in pitch angle distribution, favorable for whistler-mode wave generation, exceeds the scope of this study and needs further investigation. Accordingly, this feature resulted in an increase in anisotropy of 10-100 eV electrons (Figure 2g), which are critical for whistler wave growth with frequencies below $0.2f_{\rm ce}$, as inferred from the minimum resonance energy (E_{\min}) curves shown in Figure 2e. Correspondingly, T_{perp} became larger than T_{para} (Figure 2d) after ~05:47:00 UT. P1 observed a gradual change in Bz initiated just after the shock arrival; however, the magnitude of magnetic field remained roughly constant downstream of the shock ramp (Figure 2i). Electron fluxes over 50-500 eV (corresponding to the energies essential for wave generation below $0.1 f_{ce}$, as demonstrated in Figure 2m) increased during 05:48:00–05:53:00 UT for pitch angles close to 90°, in association with the modest enhancements in whistler wave amplitudes (Figure 2p).

3. Linear Wave Growth Analysis

To understand the whistler-mode wave generation during the IP shock events, we use the ARTEMIS observation as inputs for the generalized growth rate expression (Equation 3.9 of Kennel (1966)) to calculate wave frequency spectra of linear growth rates (Ma et al., 2014).

Figure 3 summarizes the linear growth rate calculations for the first IP shock event. We calculated linear growth rate at 0° wave normal angle, based on the wave properties analyzed using the SCM waveform data (see Figure S2 in Supporting Information S1). Figures 3a and 3b show the electron velocity distribution functions (VDF) calculated based on the observed electrons over 10 eV-1.5 keV energies just before and after the shock arrival. The electron VDF was calculated using 2D interpolation of the observed electron flux at different energies and pitch angles. Right after the shock arrival, the electron PSD decreased (increased) anti-parallel (perpendicular) to the background magnetic field. The drop in the anti-parallel PSD can be explained by the lunar surface absorption or reflection/backscattering of incoming shock-driven electrons that travel along the background magnetic field line, which is directed toward the lunar surface and connected to it. Using the electron VDFs, we calculated the linear wave growth rate at the given times and compared it with the observed wave intensity, as shown in Figures 3e and 3f. The growth rate was calculated in terms of convective wave growth per R_L (dB/ R_L). The black dotted and dashed lines on the VDFs correspond to the parallel cyclotron resonance velocity at the minimum and maximum frequencies, respectively, where significant growth rate (greater than 1) is achieved. Therefore, the electrons between the dashed and dotted lines are mainly responsible for wave growth. Figures 3e and 3f show an increase in growth rate after the shock arrival, which agrees with the observed wave intensification. The minimum resonance energy labeled in Figures 3e and 3f is calculated at the frequency of the highest positive growth rate.

Similarly, we calculated the electron VDFs and linear growth rate, as observed by P1 (see Figures 3c, 3d, 3g and 3h). The comparison of Figures 3c and 3d indicates an increase in the perpendicular PSD after the shock arrival, which led to a positive growth rate over 20–90 Hz. Since the Fast Fourier Transform (FFT) wave data before the shock arrival was not available for P2, the wave frequency spectrograms from both the Filter Bank Spectra (FBK) and FFT data products observed by P2 and P1 are presented in Figures 3i, 3j, 3l and 3m. Figures 3k and 3n show the frequency spectrogram of linear wave growth rate calculated using electrons with energies over $10 \, \text{eV} - 23 \, \text{keV}$. Figures 3j and 3k demonstrate that the calculated linear growth rate agrees with the observed wave spectra downstream of the shock ramp. The calculations show significant growth above $0.1 \, f_{\text{ce}}$ (~50 Hz), corresponding to whistler-mode waves. Another branch of waves was observed below 50 Hz, but the corresponding whistler-mode wave growth rates are small after the shock arrival. Compared with the FBK wave data before the shock arrival (Figure 3i), we find that the growth rate calculations can explain the observed waves below $0.1 \, f_{\text{ce}}$ to some extent. For P1, we find that some agreement exists between the growth rate and observed wave intensity during $04:42-04:43 \, \text{UT}$. The lower

PRASAD ET AL. 5 of 9

19448007, 2024, 10, Downloaded from https://agupubs.onlinelibrary.wiley.com/doi/10.1029/2023GL107392 by Boston University, Wiley Online Library on [31/05/2025]. See the Terms and Conditions (https://onlinelibrary.wiley.com/term

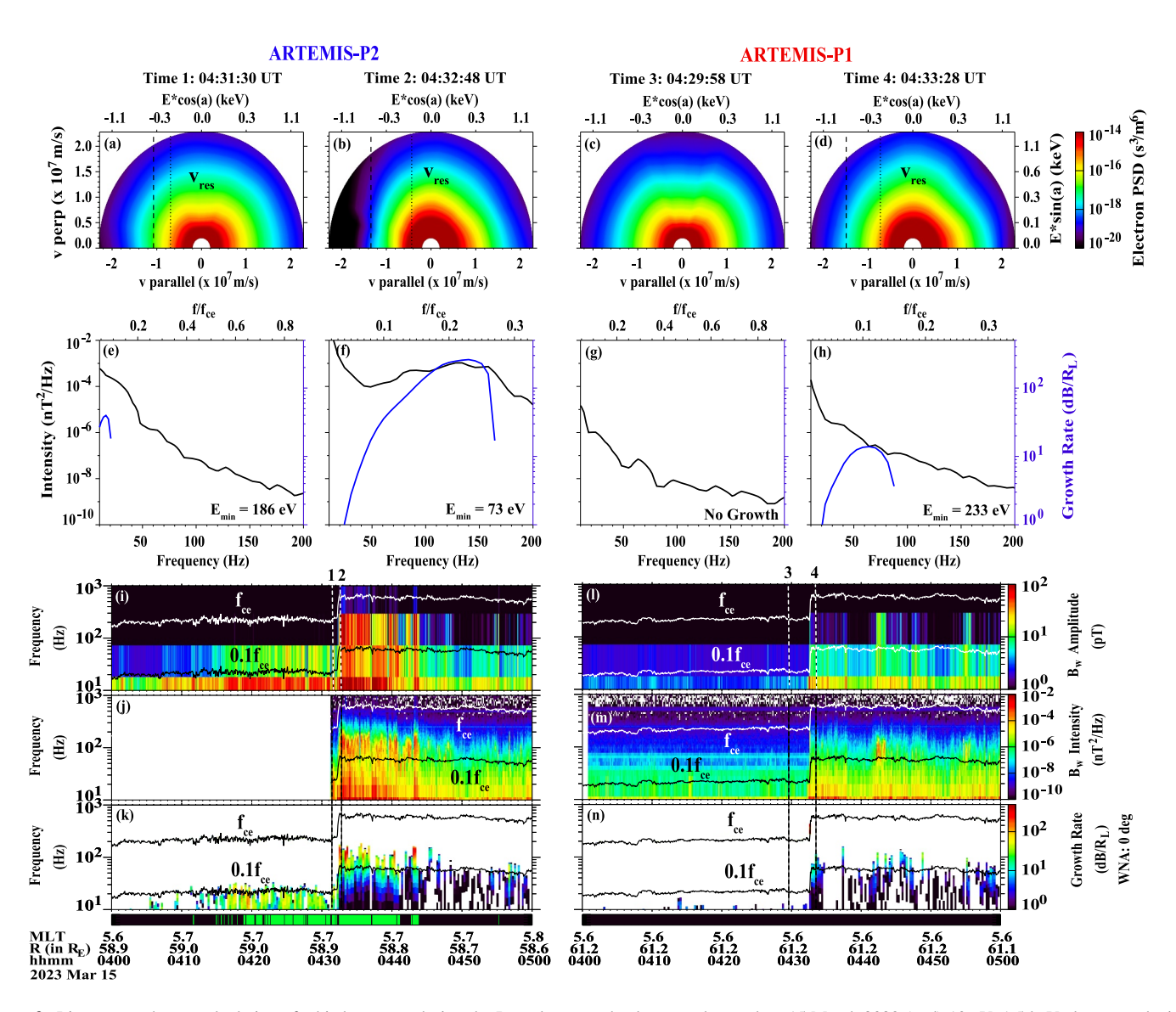


Figure 3. Linear growth rate calculation of whistler waves during the Interplanetary shock event observed on 15 March 2023 (a–d) 10 eV–1.5 keV electron velocity distribution functions (e–h) linear growth rate (blue line) and observed magnetic wave intensity (black line) as a function of frequency (i, l) frequency spectrograms of wave magnetic amplitude (j, m) magnetic power spectral density from the Fast Fourier Transform data products (k, n) frequency spectrogram of linear wave growth rate calculated using electrons with energies over 10 eV–23 keV; colorbars at the bottom of figure are an indicator of the magnetic field connection to the Moon.

growth rate for P1 compared to P2 indicates that the magnetic field line connection has played an important role in enhancing the existing anisotropies of the hot electrons, thus providing favorable conditions for whistler-mode wave generation. Overall, the linear growth rate calculations well explain the whistler-mode wave generation under the given shock conditions, highlighting the importance of pitch angle anisotropy and flux of source electrons, as well as magnetic field line connection to the Moon as the key conditions for wave intensification.

Figure 4 shows similar linear growth rate calculations for the second IP shock event. The VDFs in the top row show the electron distribution with energies up to 500 eV. Using the VDFs observed by the ESA instrument, we calculate the linear wave growth rate for the parallel waves. The calculation results are able to reproduce the wave intensification over 30–60 Hz (Figure 4f) and near 20 Hz (Figure 4h). Figures 4j and 4l show the frequency spectrograms of wave growth rates calculated using 10 eV–23 keV electron distributions. The comparison between Figures 4i and 4j demonstrates reasonably good agreement between the observed wave intensity during 05:48:00–05:52:00 UT and the corresponding linear growth rate. The rising frequency feature shown in Figure 4j during 05:47:00–05:48:00 UT, which was not evident in the observed wave spectra, may be attributed to the wave

PRASAD ET AL. 6 of 9

19448007, 2024, 10, Downloaded from https://agupubs.onlinelibrary.wiley.com/doi/10.1029/2023GL107392 by Boston University, Wiley Online Library on [31/05/2025]. See the Terms and Conditions (https://onlineli

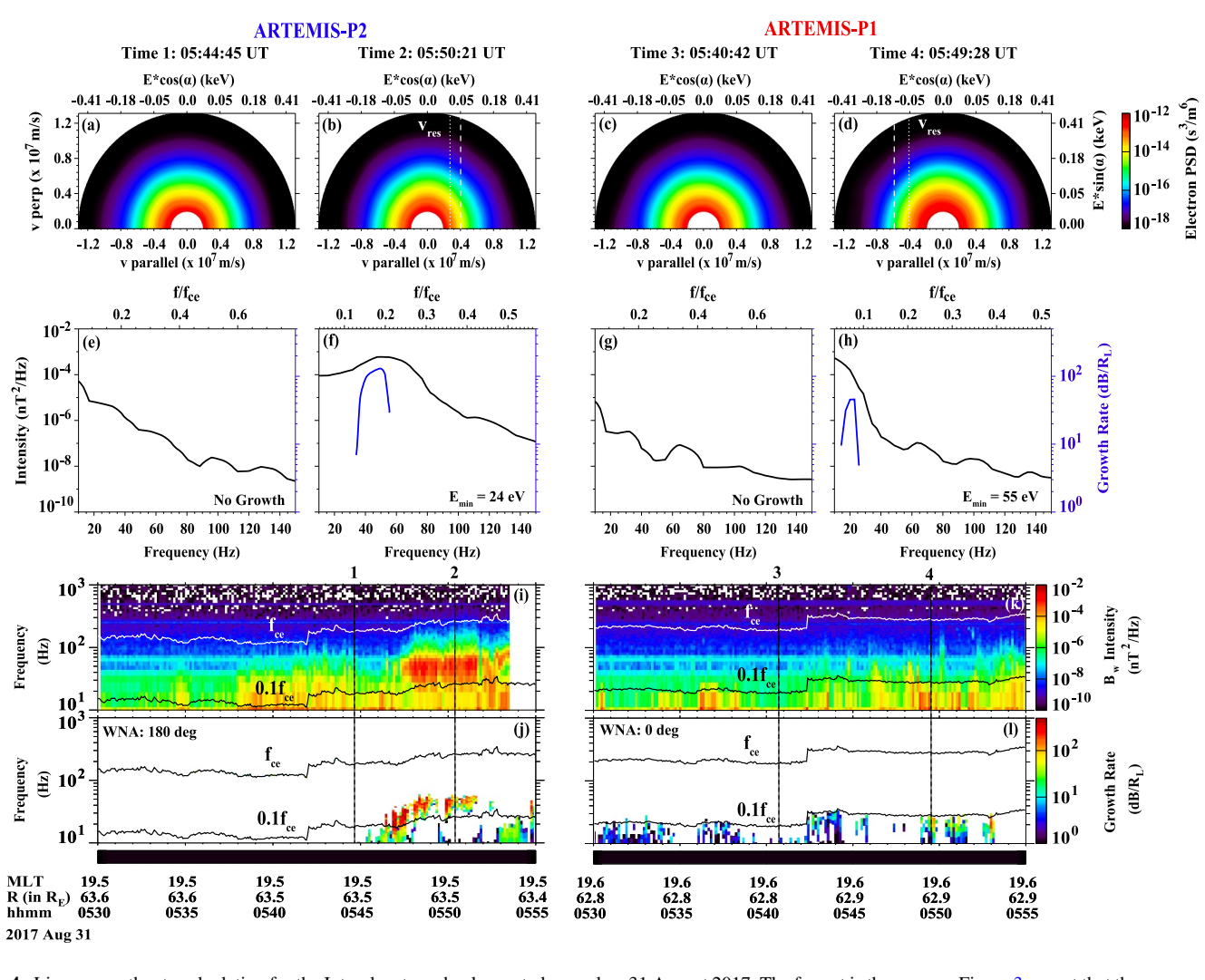


Figure 4. Linear growth rate calculation for the Interplanetary shock event observed on 31 August 2017. The format is the same as Figure 3 except that the energy range is 10–500 eV in panels (a)–(d).

propagation effect or the limitations of 2D interpolation in accurately representing electron VDF around magnetic field line rotation. The strong wave intensities below $0.1\,f_{\rm ce}$ observed by P1 during 05:49:00–05:50:00 UT and 05:50:40–05:51:30 UT are also well reproduced by the linear growth rate calculation. Thus, we conclude that the anisotropic electron pitch angle distribution could provide an energy source to generate whistler-mode waves observed by both ARTEMIS probes. Moreover, the potential magnetic field line rotation following the IP shock affects the electron pitch angle distribution, thus generating the resultant whistler-mode waves.

4. Summary and Discussion

We analyzed two IP shock events simultaneously observed by both ARTEMIS probes in the lunar plasma environment. Our study provides new insights into the potential mechanisms by which IP shocks can generate intense whistler-mode waves in the vicinity of the Moon. Using the linear wave growth theory (Kennel, 1966), we calculated the growth rate of the whistler-mode waves before and after the shock arrival, resulting in an overall good agreement with the observed wave spectra. Our primary findings are summarized below.

The first shock event demonstrates that IP shocks in the lunar environment can enhance the local pitch angle
anisotropies of electrons across the shock ramp, thus resulting in the generation of intense whistler-mode
waves. The calculated linear growth rate of whistler-mode waves based on the observed plasma parameters

PRASAD ET AL. 7 of 9



Acknowledgments

Grants 80NSSC20K0196.

The authors acknowledge the NASA

80NSSC20K0698, 80NSSC23K0410,

80NSSC22K1638, 80NSSC23K0096,

NSF Grants AGS-2225445 and AGS-

Angelopoulos for use of data from the

Specifically, we acknowledge C. W.

contract NAS5-02099 and V.

THEMIS/ARTEMIS Mission.

FGM data

80NSSC24K0239, 80NSSC24K0572 and

2247774. The authors acknowledge NASA

Carlson and J. P. McFadden for use of ESA

data, J. W. Bonnell and F. S. Mozer for use of EFI data. O. LeContel and A. Roux for

use of SCM data and K. H. Glassmeier, U.

Auster and W. Baumiohann for the use of

Geophysical Research Letters

10.1029/2023GL107392

- overall reproduces the observed wave spectra, suggesting that these whistler-mode waves are locally amplified.
- During the second shock event, magnetic field line rotation was observed downstream of the shock ramp. This
 magnetic field rotation was closely correlated with the transition of electron pitch angle distribution from a
 field-aligned to a pancake distribution, which is more favorable for whistler-mode wave generation.
- When comparing both shock events, we find that electron temperature anisotropy is not always a determining factor for whistler-mode wave generation under shock conditions. Moreover, the pitch angle anisotropy can be vastly different between low-energy and high-energy electrons. It is primarily the pitch angle anisotropy of electrons above the minimum resonance energy that plays a pivotal role in whistler wave generation, and this aspect is not always accurately reflected in temperature anisotropy.

It is important to note that our study does not assume linear instability as the sole factor governing the entire wave growth and spectra. Instead, we acknowledge the potential role of nonlinear effects in the chorus wave growth process. Nevertheless, it is known that these nonlinear processes start with seed waves with frequencies near the maximum linear growth (Omura et al., 2008). Hence, linear wave growth rate provides a valuable proxy to estimate the approximate wave frequency range where positive wave growth is feasible.

In this study, we provide insights into the potential mechanisms under which whistler-mode waves are generated around the Moon under shock conditions. It will be particularly interesting to delve deeper into the various mechanisms through which IP shocks can develop new pitch angle anisotropies in the local plasma, ultimately leading to whistler-mode wave generation. Our results indicate that IP shocks can create disturbances in the background magnetic field, developing sharp local gradients that can lead to anisotropic electron distribution. Whistler-mode wave generation around local inhomogeneties of magnetic field in the form of dips or jumps in magnitude or sudden field line rotation has been observed in the Earth's magnetosheath and solar wind (Ahmadi et al., 2018; Artemyev et al., 2019; Karbashewski et al., 2023). It will also be interesting to further examine the precise mechanism for changes in pitch angle distributions around magnetic field line rotation that can lead to whistler-mode wave generation.

Finally, to determine the role of IP shocks in developing suitable plasma conditions for whistler-mode wave intensification, it will be interesting to conduct a more comprehensive statistical study by analyzing multiple shock events in the lunar environment and characterizing the plasma conditions around the shock region.

Data Availability Statement

Acceleration, Reconnection, Turbulence and Electrodynamics of the Moons Interaction with the Sun data is publicly available at https://artemis.igpp.ucla.edu/. The WIND magnetic field investigation data is publicly available at NASA Space Physics Data Facility (SPDF) via https://doi.org/10.48322/av38-wn55 (Koval et al., 2021). WIND 3D Particle Analyzers data is publicly available at NASA SPDF via https://doi.org/10.48322/s8e6-aw08 (Lin et al., 2021). The data used to produce figures in the present study are publicly available in figshare via https://doi.org/10.6084/m9.figshare.24312520.v2.

References

Ahmadi, N., Wilder, F. D., Ergun, R. E., Argall, M., Usanova, M. E., Breuillard, H., et al. (2018). Generation of electron whistler waves at the mirror mode magnetic holes: MMS observations and PIC simulation. *Journal of Geophysical Research: Space Physics*, 123(8), 6383–6393. https://doi.org/10.1029/2018JA025452

Angelopoulos, V. (2011). The ARTEMIS mission. Space Science Reviews, 165(1), 3-25. https://doi.org/10.1007/s11214-010-9687-2

Artemyev, A. V., Angelopoulos, V., Vasko, I. Y., Runov, A., Avanov, L. A., Giles, B. L., et al. (2019). On the kinetic nature of solar wind discontinuities. *Geophysical Research Letters*, 46(3), 1185–1194. https://doi.org/10.1029/2018GL079906

Auster, H. U., Glassmeier, K. H., Magnes, W., Aydogar, O., Baumjohann, W., Constantinescu, D., et al. (2008). The THEMIS fluxgate magnetometer. Space Science Reviews, 141(1), 235–264. https://doi.org/10.1007/s11214-008-9365-9

Bonnell, J. W., Mozer, F. S., Delory, G. T., Hull, A. J., Ergun, R. E., Cully, C. M., et al. (2008). The electric field instrument (EFI) for THEMIS. Space Science Reviews, 141(1), 303–341. https://doi.org/10.1007/s11214-008-9469-2

Chen, M. W., Roeder, J. L., Fennell, J. F., Lyons, L. R., Lambour, R. L., & Schulz, M. (1999). Proton ring current pitch angle distributions: Comparison of simulations with CRRES observations. *Journal of Geophysical Research*, 104(A8), 17379–17389. https://doi.org/10.1029/1999JA900142

Davis, L. A., Cattell, C. A., Wilson, L. B., Cohen, Z. A., Breneman, A. W., & Hanson, E. L. M. (2021). ARTEMIS observations of plasma waves in Laminar and perturbed interplanetary shocks. The Astrophysical Journal, 913(2), 144. https://doi.org/10.3847/1538-4357/abf56a

Fatemi, S., Holmström, M., Futaana, Y., Barabash, S., & Lue, C. (2013). The lunar wake current systems. *Geophysical Research Letters*, 40(1), 17–21. https://doi.org/10.1029/2012GL054635

PRASAD ET AL. 8 of 9

- Gurnett, D. A., & Bhattacharjee, A. (2017). Introduction to plasma physics: With space, laboratory and astrophysical applications (2nd ed.). Cambridge University Press. https://doi.org/10.1017/9781139226059
- Halekas, J. S., Bale, S. D., Mitchell, D. L., & Lin, R. P. (2005). Electrons and magnetic fields in the lunar plasma wake. *Journal of Geophysical Research*, 110(A7), A07222. https://doi.org/10.1029/2004JA010991
- Halekas, J. S., Brain, D. A., Mitchell, D. L., & Lin, R. P. (2006). Whistler waves observed near lunar crustal magnetic sources. Geophysical Research Letters, 33(22), L22104. https://doi.org/10.1029/2006GL027684
- Halekas, J. S., Brain, D. A., Mitchell, D. L., Lin, R. P., & Harrison, L. (2006). On the occurrence of magnetic enhancements caused by solar wind interaction with lunar crustal fields. Geophysical Research Letters, 33(8), L08106. https://doi.org/10.1029/2006GL025931
- Halekas, J. S., Poppe, A. R., Farrell, W. M., Delory, G. T., Angelopoulos, V., McFadden, J. P., et al. (2012). Lunar precursor effects in the solar wind and terrestrial magnetosphere. *Journal of Geophysical Research*, 117(A5). https://doi.org/10.1029/2011JA017289
- Halekas, J. S., Saito, Y., Delory, G. T., & Farrell, W. M. (2011). New views of the lunar plasma environment. *Planetary and Space Science*, 59(14), 1681–1694. https://doi.org/10.1016/j.pss.2010.08.011
- Harada, Y., & Halekas, J. S. (2016). Upstream waves and particles at the moon. In A. Keiling, D.-H. Lee, & V. Nakariakov (Eds.), Geophysical Monograph Series (pp. 307–322). John Wiley & Sons, Inc. https://doi.org/10.1002/9781119055006.ch18
- Harada, Y., Halekas, J. S., Poppe, A. R., Kurita, S., & McFadden, J. P. (2014). Extended lunar precursor regions: Electron-wave interaction. Journal of Geophysical Research: Space Physics, 119(11), 9160–9173. https://doi.org/10.1002/2014JA020618
- Harada, Y., Halekas, J. S., Poppe, A. R., Tsugawa, Y., Kurita, S., & McFadden, J. P. (2015). Statistical characterization of the foremoon particle and wave morphology: ARTEMIS observations. *Journal of Geophysical Research: Space Physics*, 120(6), 4907–4921. https://doi.org/10.1002/ 2015JA021211
- Harten, R., & Clark, K. (1995). The design features of the GGS wind and polar spacecraft. Space Science Reviews, 71(1), 23–40. https://doi.org/10.1007/BF00751324
- Hood, L. L., Torres, C. B., Oliveira, J. S., Wieczorek, M. A., & Steward, S. T. (2020). Lunar crustal magnetic field map. https://doi.org/10.17189/ 1520494
- Kajdič, P., Blanco-Cano, X., Aguilar-Rodriguez, E., Russell, C. T., Jian, L. K., & Luhmann, J. G. (2012). Waves upstream and downstream of interplanetary shocks driven by coronal mass ejections. *Journal of Geophysical Research*, 117(A6), A06103. https://doi.org/10.1029/20111A017381
- Kajdič, P., Lavraud, B., Zaslavsky, A., Blanco-Cano, X., Sauvaud, J.-A., Opitz, A., et al. (2014). Ninety degrees pitch angle enhancements of suprathermal electrons associated with interplanetary shocks. *Journal of Geophysical Research: Space Physics*, 119(9), 7038–7060. https://doi.org/10.1002/2014JA020213
- Karbashewski, S., Agapitov, O. V., Kim, H. Y., Mozer, F. S., Bonnell, J. W., Froment, C., et al. (2023). Whistler wave observations by Parker solar probe during encounter 1: Counter-propagating whistlers Collocated with magnetic field inhomogeneities and their application to electric field measurement calibration. The Astrophysical Journal, 947(2), 73. https://doi.org/10.3847/1538-4357/acc527
- Kennel, C. (1966). Low-frequency whistler mode. The Physics of Fluids, 9(11), 2190-2202. https://doi.org/10.1063/1.1761588
- Koval, A., Lepping, R. P., & Szabo, A. (2021). Wind magnetic field investigation (MFI) composite data [Dataset]. NASA Space Physics Data Facility. https://doi.org/10.48322/AV38-WN55
- Lepping, R. P., Acūna, M. H., Burlaga, L. F., Farrell, W. M., Slavin, J. A., Schatten, K. H., et al. (1995). The WIND magnetic field investigation. Space Science Reviews, 71(1), 207–229. https://doi.org/10.1007/BF00751330
- Lin, R. P., Bale, S. D., & Wilson, III, L. B. (2021). Wind 3DP PESA Moments data NASA space Physics data Facility space Sciences Laboratory [Dataset]. *University of California*. https://doi.org/10.48322/S8E6-AW08
- Ma, Q., Li, W., Chen, L., Thorne, R. M., & Angelopoulos, V. (2014). Magnetosonic wave excitation by ion ring distributions in the Earth's inner magnetosphere. *Journal of Geophysical Research: Space Physics*, 119(2), 844–852. https://doi.org/10.1002/2013JA019591
- Means, J. D. (1972). Use of the three-dimensional covariance matrix in analyzing the polarization properties of plane waves. *Journal of Geophysical Research*, 77(28), 5551–5559. https://doi.org/10.1029/JA077i028p05551
- Nakagawa, T. (2016). ULF/ELF waves in near-moon space. In A. Keiling, D.-H. Lee, & V. Nakariakov (Eds.), Geophysical Monograph Series (pp. 293–306). John Wiley & Sons, Inc. https://doi.org/10.1002/9781119055006.ch17
- Nakagawa, T., & Iizima, M. (2005). Pitch angle diffusion of electrons at the boundary of the lunar wake. Earth Planets and Space, 57(9), 885–894. https://doi.org/10.1186/BF03351866
- Nakagawa, T., Takahashi, F., Tsunakawa, H., Shibuya, H., Shimizu, H., & Matsushima, M. (2011). Non-monochromatic whistler waves detected by Kaguya on the dayside surface of the moon. *Earth Planets and Space*, 63(1), 37–46. https://doi.org/10.5047/eps.2010.01.005
- Omura, Y., Katoh, Y., & Summers, D. (2008). Theory and simulation of the generation of whistler-mode chorus. *Journal of Geophysical Research*, 113(A4), A04223. https://doi.org/10.1029/2007JA012622
- Roux, A., Le Contel, O., Coillot, C., Bouabdellah, A., de la Porte, B., Alison, D., et al. (2008). The Search Coil magnetometer for THEMIS. Space Science Reviews. 141(1), 265–275. https://doi.org/10.1007/s11214-008-9455-8
- Russell, C. T., Jian, L. K., Blanco Cano, X., Luhmann, J. G., & Zhang, T. L. (2009). STEREO observations of shock formation in the solar wind. Geophysical Research Letters, 36(2), L02103. https://doi.org/10.1029/2008GL036337
- Sawaguchi, W., Harada, Y., & Kurita, S. (2021). Discrete rising tone elements of whistler-mode waves in the vicinity of the Moon: ARTEMIS observations. *Geophysical Research Letters*, 48(1), e2020GL091100. https://doi.org/10.1029/2020GL091100
- Sawaguchi, W., Harada, Y., Kurita, S., & Nakamura, S. (2022). Spectral properties of whistler-mode waves in the vicinity of the Moon: A statistical study with ARTEMIS. *Journal of Geophysical Research: Space Physics*, 127(9), e2022JA030582. https://doi.org/10.1029/2022JA030582
- Sonnerup, B. U. Ö., & Cahill, Jr, L. J. (1967). Magnetopause structure and attitude from Explorer 12 observations. *Journal of Geophysical Research*, 72(1), 171–183. https://doi.org/10.1029/JZ072i001p00171
- Tong, Y., Vasko, I. Y., Artemyev, A. V., Bale, S. D., & Mozer, F. S. (2019). Statistical study of whistler waves in the solar wind at 1 au. *The Astrophysical Journal*, 878(1), 41. https://doi.org/10.3847/1538-4357/ab1f05
- Tong, Y., Vasko, I. Y., Pulupa, M., Mozer, F. S., Bale, S. D., Artemyev, A. V., & Krasnoselskikh, V. (2019). Whistler wave generation by Halo electrons in the solar wind. *The Astrophysical Journal*, 870(1), L6. https://doi.org/10.3847/2041-8213/aaf734
- Tsugawa, Y., Terada, N., Katoh, Y., Ono, T., Tsunakawa, H., Takahashi, F., et al. (2011). Statistical analysis of monochromatic whistler waves near the Moon detected by Kaguya. *Annales Geophysicae*, 29(5), 889–893. https://doi.org/10.5194/angeo-29-889-2011
- Wilson, III, L. B., Koval, A., Szabo, A., Breneman, A., Cattell, C. A., Goetz, K., et al. (2013). Electromagnetic waves and electron anisotropies downstream of supercritical interplanetary shocks. *Journal of Geophysical Research: Space Physics*, 118(1), 5–16. https://doi.org/10.1029/ 20121A018167

PRASAD ET AL. 9 of 9